Nucleation and propagation of dislocations during nanopore lattice mending by laser annealing: Modified continuum-atomistic modeling

Pei-Hsing Huang and Hsin-Yi Lai*
Department of Mechanical Engineering, National Cheng-Kung University, Tainan 701, Taiwan
(Received 5 October 2007; revised manuscript received 31 December 2007; published 10 March 2008)

This paper investigates the atomic-level microscopic dynamic behavior of a solid-state nanopore lattice mending process by femtosecond laser annealing using a modified continuum-atomistic modeling approach. The nucleation and propagation of dislocation are also depicted via quantitative dislocation analyses. Three typical lattice mending phases, including (i) the incubation of dislocation nucleation, (ii) pressure-induced dislocation propagation and plastic deformation, and (iii) lattice recovery and reconstruction via thermal diffusion, are thoroughly characterized by the evolution of microscopic dislocation and the slope change of atomic mean-squared displacement curve. The results of the analyses indicate that the structural mending originated from the heterogeneous nucleation of dislocation from the pore surface. The laser-induced shock waves provide considerable mechanical work and, consequently, are transferred largely to become an equivalent applied stress on the activated glide planes. These pressure-induced multiple glides on a lattice near the pore rapidly and effectively enable the mending operations in solid-state structural transition processes. Subsequently, the relaxation of the compression stress leads to the target material that is rapidly swelled in the z direction with an expansive strain rate of 2.2×10^{9} s^{-1}. The expansion dynamics and associated tension stress further induce drastic emissions of dislocation after the pore is completely mended. Moreover, it is also observed that the dislocation of sessile stair rods can act as a strong barrier to prevent further glide on slip planes, thus leading to a local strain-hardening effect. The simulation results presented in this paper provide comprehensive insights for a better understanding of the laser-induced solid-state nanopore mending process. The approach proposed here can also be modified and used to further investigate the mechanisms of laser-induced surface hardening with various advanced functional materials.

DOI: 10.1103/PhysRevB.77.125408 PACS number(s): 61.72.Cc, 61.72.−y, 61.80.Ba, 61.50.Ks

I. INTRODUCTION

Nanopores, chinks, and various microdefects are often in existence in many solid-state materials.[1,2] They are commonly innate in raw materials and often introduced in materials processing and product fabrication stages. These microdefects can substantially reduce the mechanical reliability of the related structure and can also cause considerable changes in the global physical properties of materials.[1,2] Thus, it can sometimes lead to disastrous breakdowns in electronic circuits and mechanical system and even shorten the component life of the underlying system. Conventionally, furnace annealing is used as a typical technique in the lattice mending and structural recovery. However, this technique usually does not meet the practical requirements of microscopic processing due to realistic constraints of large-scale thermal diffusions and solid solubility. The femtosecond laser annealing (FLA) technology used in semiconductor materials has generated extensive interest since the late 1970s. Several important findings have been obtained so far for this particular issue. These include sufficiently dense photoexcited plasma that can weaken the lattice structure and enhance atomic mobility without significantly increasing their thermal energy.[3] Thus, the technique was modified and used as a commercial technique to generate a high-crystallographic-quality material, such as those used in a heavily damaged silicon sample.[1,4] One may realize that a large portion of the incident energy in a femtosecond pulse laser is only confined to a region of several optical skin depths. The aforementioned invaluable traits can, therefore, be used as a well-controlled local heating zone[5] and for laser-induced nonthermal structural changes.[3,6] In view of the many advantages mentioned above, the FLA can, thus, be considered as a potential method for use in semiconductors and microelectronic industry.[1–3]

Various laser annealing techniques were used to investigate the problems associated with crystal growth, damage recovery, and preparation of alloys of nonthermodynamic compositions.[1–3,7] The time scale for this type of research problems is close to that of the natural oscillation periods of atoms and molecules. That is to say, both time scales are all from several femtoseconds ($1\ \text{fs}=10^{-15}$ s) to picoseconds ($1\ \text{ps}=10^{-12}$ s).[3,6,8] In such a short time scale, the microscopic variation involves many complicated processes including optical energy transfer, carrier dynamics, and thermal and mechanical mechanisms. However, in such a short temporal duration and spatial scales, to explore the fundamental mechanisms of aforementioned topics via experimental methods is a great challenge. Therefore, the employment of molecular dynamics (MD) simulation is indispensable for such a critical research area.

To further understand the intrinsic mechanism of short-pulse laser-induced structural changes, microscopic exploration is needed. MD simulation is one of the techniques employed for the study of laser-material interactions in the past two decades.[8–13] Since electronic thermal conduction is the major heat flux mechanism in ultrafast laser interaction with metals, classical MD simulation is based purely on the atomic contribution; direct employment of the classical MD model for laser-metal heating process may, therefore, lead to

unrealistic results. The continuum two-temperature model[14,15] (TTM) has taken both electronic and lattice heat conduction into account. The model, thus, becomes one of the popular models widely adopted for the prediction of temperature evolution in laser irradiation and process interaction with metal in recent years. The continuum TTM model, however, is subject to several intrinsic real physical limitations, including nucleation of voids, ablations, and spallation.[8–11] These microscopic behaviors can hardly be realized by using macroscopic continuum modeling and classical nucleation theory.[16,17] In view of this, the TTM and MD combined approach was proposed by Hakkinen and Landman[8] to circumvent the aforementioned technical difficulties. The TTM-MD model has been successfully used to study the laser-metal ablation mechanisms by Schafer *et al.*[9] and Ivanov and Zhigilei,[10] where the energy coupling of electrons and the lattice was considered as one additional term in the resultant force for each atom. Later on, another energy exchange method was presented by Chen and Xu,[11] Amoruso *et al.*,[13] and Wang,[18] in which the electron-phonon coupling energy was proportionally converted to the atomic velocity of the lattice subsystem with a scaling factor. Although the aforementioned MD approaches are mainly applied for laser-induced surface ablation, they can be further modified for the study of laser irradiations and interactions of microscopic defects in metal materials.

This study intends to characterize microscopic behaviors of nanopore lattice mending for femtosecond laser annealing processes. To ensure model adequacy for the study of a nonequilibrium laser heating and annealing process, a modeling scheme by using a modified atomistic-continuum model in combination with a quantitative dislocation signature is proposed in the study. Several distinct features of nanopore behaviors as subjected to the pulse laser impinging are elaborated in this study, which include the investigations of (1) microscopic origination and the structural mending mechanism of a nanopore during incipient plastic deformation period, (2) the nucleation and growth mechanisms of a dislocation, (3) the onset conditions for three mending stages induced by the variation of thermal and structural features, and (iv) the mending patterns of resulting microstructures for integrity visualization.

II. COMPUTATIONAL DESCRIPTIONS

A. Simulation setup for laser annealing process

Due to the outstanding characters of high electromigration resistance and low bulk resistivity, copper has been well recognized and adopted as one of the most popular candidates of interconnection materials.[19,20] Moreover, using the femtosecond laser ablation on copper to repair the conductor wiring and to customize the circuits have emerged as one of the important processes.[20] Because of that, the single-crystal copper is selected as the simulation material for this study.

The simulated pore in this study is actually a cylindrical-like defect, not a spherical void. Therefore, the simulation domain is adopted to characterize the evolutionary nature of the dislocation in the x-z plane with a reasonable size in the y direction. In order to obtain a better result and to avoid possible errors in the computation of atomic potential energy and forces, the dimension of the computation domain in the y direction (14.5 and 18.1 Å) is thus taken to be two times larger than that of the cutoff radius (7.2 Å) in force and energy computations. Our intention here for this analysis is to provide a clear evidence of the relevant characteristics of the laser-induced surface hardening and lattice mending processes. The proposed model presents sufficiently close to realistic scenarios by using a simulation domain with reasonable dimensions. Both phenomena obtained from the evolutionary nature of the dislocation in the x-z plane and the laser-induced lattice mending process are clearly explained, especially for the laser irradiation process occurring in such a short time period.

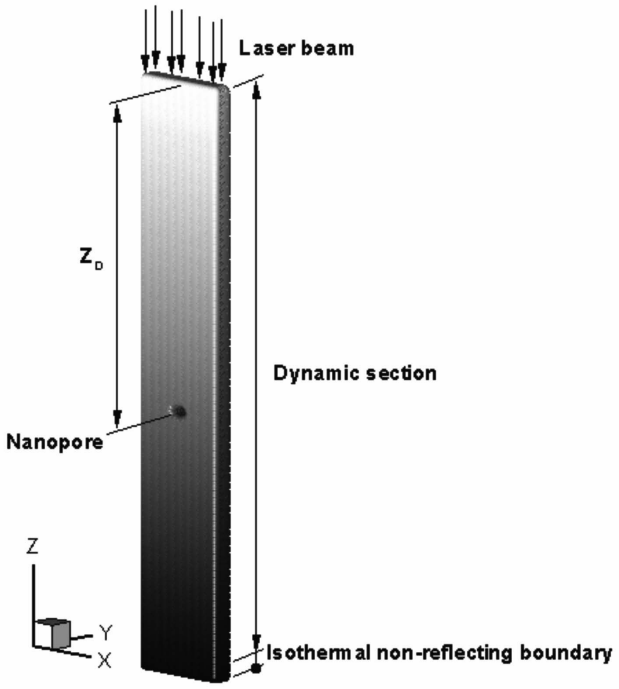

FIG. 1. Schematic illustration of the MD simulated domain.

To minimize the finite size effect, three different sizes of single-crystal copper-plate systems, including $108.4\times14.5\times903.5$, $144.56\times14.5\times903.5$, and $180.7\times18.1\times903.5$ Å^3 in the x, y, and z directions, are adopted for the study. The corresponding computational cells comprise $30a_0\times4a_0\times250a_0$, $40a_0\times4a_0\times250a_0$, and $50a_0\times5a_0\times250a_0$ face-centered cubic (FCC) unit cells (a_0=3.614 Å), respectively. The nanopore diameters of 2–5 nm are preset for simulation. The pore is located on the central axis of the copper plate at different depths of Z_D=30.4, 50.4, or 70.4 nm below the radiated surfaces, as shown in Fig. 1. Periodic boundary conditions (PBCs) are assigned to the boundaries of x and y coordinates (since a typical laser spot diameter is assumed much larger than the simulated cross-sectional area) and free boundary conditions on the top surface of the z coordinate. It is worth mentioning that the use of lateral PBC is equivalent to a periodic pore array configuration. Moreover, in order to prevent a boundary reflection of shock waves bouncing back into the simulation domain, the nonre-

flecting boundary technique[21] is adopted at the bottommost boundary to mimic the shock waves transmitted into the infinite elastic solid medium. In addition, three layers of crystals at the bottommost boundary are treated as a heat-bath-like thermostat via the Gauss principle of least constraints algorithm.[22,23] The thermostat keeps the temperature of the bottom lattices at a constant temperature of 300 K, imitating the heat diffusion outward. Above the heat bath are the so-called free motion layers or dynamic sections. The atoms in dynamic sections interact with the incoming "laser beam," transferring heat, energy, and force into the bulk materials.

In the present work, the near-infrared Ti:sapphire femtosecond laser system with pulse duration in the range of 50 ~ 125 fs and wavelength of 800 nm (1.55 eV) was adapted for simulation. The laser beam is controlled and impinged in the z direction. By assuming uniform in vacuum and Gaussian in time with a fixed full width at half-maximum of 100 fs centered at 1 ps, the total incident energy densities can be expressed in terms of absorbed laser fluence, F_{abs}, which was sequentially performed between 28.8 and 85.0 mJ/cm^2 for simulation. In the following sections, the structure made of copper materials with a nanopore of 3.0 nm in diameter and located at the vertical depth of 50.4 nm underneath the irradiated surface is used as an example to illustrate the efficiency and accuracy of the proposed modeling approach.

B. Laser energy deposition description

High-intensity short-pulse laser irradiation on a metallic substrate results in extreme electronic temperatures in the vicinity of the surface. In metal materials, the specific heat capacity of electrons is much lower than that of the phonons in the same specimen, thus, the instantaneous temperature increase for electrons will be much faster than for phonons. This can lead to the temperature of electrons and the lattice being inequivalent at the initial heating stage. In case the laser pulse duration is shorter than the relaxation time between electrons and the lattice, the nonequilibrium heating process can thus be induced. The TTM was first presented by Kaganov *et al.*[14] in 1957 and by Anisimov *et al.*[15] in 1974. Since then the model has emerged as a popular model for use in modeling such a nonequilibrium heating process, where hot electron baths in the cold lattice are described by two separate subsystems of electron and lattice temperatures, T_e and T_l, respectively. Later on, Qiu and Tien[24] came up with a hyperbolic two-step radiation-heating model by solving the Boltzmann transport equation from quantum mechanical considerations. It has been concluded that if the laser pulse duration is much longer than the electronic relaxation time, then the nonequilibrium among electrons can be ignored.[25] Typically for noble metals, the electronic relaxation time τ_e at room temperature and above is less than 30 fs.[25] Therefore, in the case of the femtosecond laser (typically, 100 ~ 500 fs) interacting with a noble metal, the nonequilibrium effect among electrons can be ignored. Moreover, the dimension of the laser spot size is typically much larger than that of the heat penetration depth. Such a heating process can thus be described by a one-dimensional version of TTM model. The model is given as

$$C_e(T_e)\frac{\partial T_e}{\partial t} = \frac{\partial}{\partial z}\left[K_e(T_e,T_l)\frac{\partial T_e}{\partial z}\right] - G(T_e - T_l) + S(z,t), \tag{1}$$

$$C_l\frac{\partial T_l}{\partial t} = G(T_e - T_l), \tag{2}$$

where C and K are the heat capacities and thermal conductivities of electrons and the lattice as denoted by subscripts of e and l, and G is the electron-phonon coupling factor. The laser heating source term, $S(z,t)$, is used to describe the deposition of local laser energy in different target depths and time steps in a laser pulse irradiation process. $S(z,t)$ is assumed to be a Gaussian temporal profile and is modulated by the Beer–Lambert law to produce the energy deposited by exponential decay in the direction of incident light. The associated equation can be described by

$$S(z,t) = I_0(1 - R - T)D_p^{-1}e^{-z/D_p}e^{-(t-t_0)^2/2\sigma^2}, \tag{3}$$

where I_0 is the peak intensity, and R and T denote reflectivity and transmissivity, respectively. D_p is the optical penetration depth and t_0 is the time at the peak of incident pulse power distribution. σ is the standard deviation of the Gaussian profile, which is related to t_p by $\sigma = t_p/\sqrt{8\ln 2}$.

By solving the continuum governing Eqs. (1)–(3), the time evolutions of the temperatures for electrons and the lattice can be obtained analytically. Since Eq. (1) is highly nonlinear, the *Crank–Nicholson* approach[26] is then employed for numerical computation. The time step in terms of finite difference (FD) representation, Δt_{FD}, shall be taken reasonably small as compared to that of $C_e(T_e)(\Delta x_{\text{FD}})^2/[2K_e(T_e,T_l)] \approx 25$ as (10^{-18} s) in order to ensure numerical stability. The length of the grid spacing (Δx_{FD}), equal to the atomic potential cutoff distance, is also adopted. The number of grid points is increased or decreased proportionally to meet the resolution requirement of lattice expansion and condensation processes.

In the present work, the single-crystal copper is selected as the radiated target. On the fresh copper surface, the theoretical reflectance R induced by a radiation of wavelength 800 nm (1.55 eV) is 0.961, the optical penetration depth D_p is 12.6 nm,[27] and the transmissivity T is ignored here (i.e., assuming the material is in a semi-infinite thickness). The specific heat of electrons is taken as $C_e = \gamma T_e$, $\gamma = 96.6$ J m^{-3} K^{-2}, and $C_l = 3.5\times 10^6$ J m^{-3} K^{-1}.[28] A general accepted G value of 1×10^{17} W K^{-1} m^{-3} is adopted.[29] The temperature dependence of electronic heat conductivity, $K_e(T_e,T_l)$, is employed based on the following relations[9,30]:

$$K_e = a\vartheta_e(\vartheta_e^2 + 0.16)^{1.25}(\vartheta_e^2 + 0.44)(\vartheta_e^2 + 0.092)^{-0.5} \times (\vartheta_e^2 + b\vartheta_l)^{-1}, \tag{4}$$

where $\vartheta_e = T_e/T_F$, $\vartheta_l = T_l/T_F$, and $T_F = 8.12\times 10^4$ K (Ref. 31) is the Fermi temperature of copper. Coefficients a and b are equal to 377 W K^{-1} m^{-1} and 0.139, respectively.[9]

C. Modified continuum-atomistic approach

The modified continuum-atomistic approach that combines the continuum TTM with MD simulation is elaborately proposed to treat the problem of nonequilibrium heating in this study. The MD simulation is performed via an initial state of *NPT* ensemble. The Morse potential was already used by other authors, with good agreement between the numerical and the experimental results for noble metals,[11,32,33] and it has been widely used to study the laser-metal interaction in different laser applications.[11,13,18,32,33] We have, therefore, considered the Morse potential for the present study because its simpler form allows us to use a relatively larger system and an extension of the simulation time. According to the Morse potential, the interaction energy $\phi(r_{ij})$ between two atoms i and j separated by a distance r_{ij} is given by[34]

$$\phi(r_{ij}) = D\{\exp[-2\alpha(r_{ij}-r_0)] - 2\exp[-\alpha(r_{ij}-r_0)]\}, \quad (5)$$

and the corresponding intermolecular forces $F(r_{ij})$ are

$$F(r_{ij}) = 2\alpha D\{\exp[-2\alpha(r_{ij}-r_0)] - \exp[-\alpha(r_{ij}-r_0)]\}, \quad (6)$$

where D is the total dissociation energy, α is a constant which is dependent on the material, and r_0 is the equilibrium distance, with values of 5.2587×10^{-13} erg, 1.3123 Å^{-1}, and 2.8985 Å, respectively.[34] The atomic potential and intermolecular forces of the system are derived in each computational time step of Δt_{MD}=5 fs. The cutoff radius (potential cutoff), r_c, is taken as $2.5r_0$, which is commonly adopted in MD simulations of the Morse potential. To save computational time, the comparison of the atomic distance with r_c is organized using the cell structure and linked list method.[35] Moreover, the atomic velocities and accelerations are accurately estimated by means of Gear's fifth-order predictor-corrector algorithm.[35]

In this work, the irradiated target made of copper materials is divided into a set of *computational grids* with each *cells* perpendicular to the incident beam in the z direction. The thickness of each cell is set to the cutoff distance r_c. The estimation of thermodynamic properties is also performed in terms of the equivalent averaged value of all cell atoms for each evaluated cell. The pressure P is estimated by the sum of momentum flux that is induced by atomic motions and intermolecular forces, which is derived from the virial theory.[35] The lattice temperature T_l of the MD system is calculated by using the atomic thermal vibration formulas

$$T_l(z) = \frac{m}{3N(z)k_B}\sum_{i=1}^{N(Z)}\left[\sum_{\alpha=1}^{3}(v_{i,\alpha}-\bar{v}_\alpha)^2\right] \quad (7)$$

and

$$P = \rho k_B T_l(z) + \frac{1}{3V}\left\langle\sum_{i=1}^{N(Z)}\sum_{j<i}\vec{F}_{ij}\cdot\vec{r}_{ij}\right\rangle, \quad (8)$$

where $N(z)$ is the total number of atoms for an evaluated cell located at position z and V denotes the volume occupied by the cell atoms. k_B is the Boltzmann constant and m is the mass of the atom. α represents the spatial coordinates (x, y, and z when α=1, 2, and 3, respectively), $v_{i,\alpha}$ is the velocity of atom i at the αth coordinate, and $\bar{v}_\alpha$ is the averaged velocity of atoms at the αth coordinate. Both continuum electrons and the lattice temperature can be obtained via solving the continuum TTM governing Eqs. (1) and (2) with thermal-insulation boundary conditions in each finite difference time step (Δt_{FD}=25 as). New atomic velocities can then be derived in terms of energy scaling between the variations of continuum lattice temperature and the atomic vibration kinetic energy in the MD system, which is fulfilled by scaling the velocity of atoms with a scaling coefficient ξ as follows:

$$\xi(z) = \left[1 + \frac{[C_l\Delta T_l(z)\rho_r]V_{cell}}{\frac{1}{2}m\sum_{i=1}^{N(z)}\sum_{\alpha=1}^{3}(v_{i,\alpha}-\bar{v}_\alpha)^2}\right]_{cell}^{1/2} \quad (9)$$

and

$$v_{i,\alpha}^{new} = (v_{i,\alpha}-\bar{v}_\alpha)\xi(z) + \bar{v}_\alpha, \quad \alpha = 1,2,3, \quad (10)$$

where $\rho_r=\rho(z)/\rho_{\text{ave}}$. $\rho(z)$ and ρ_{ave} denote the atomic number density of both the evaluated local cell and the bulk average, respectively. ΔT_l stands for the variations of the lattice temperature within two consecutive MD time steps. Moreover, the lattice and electronic temperature distributions are updated carefully after finishing each MD calculation step. The detailed flowchart of the modified continuum-atomistic model is shown in Fig. 2.

It should be noted that the scaling coefficient ξ is obtained by using the principle of energy conservation expressed in terms of atomic density distribution in the region where the variations of lattice energy (induced by coupled electron-phonon energy estimated by TTM model) are turned into atomic kinetic energy. The equivalent energy conversion in terms of scaling factor is physically sound and can, thus, be used in MD simulation. In MD simulation process, various structural evolutionary characters, including spallation and void formation, can possibly reduce local atomic density and eventually lead to material noncontinuum or nonhomogeneity. Thus, in the neighborhood of the nanopore, region of spallation, and top surfaces, the adaptation of "inhomogeneous" computational cells becomes necessary. If the lattice energy variations are directly scaled and added to the atomic kinetic energy of these inhomogeneous cells without considering the effect of atomic density, it apparently will lead to an unphysical result of "temperature jump" in these cells due to the redistribution of the variations of the lattice energy to fewer atoms of these low-atomic-density cells. In order to avoid an erroneous estimation of energy deposition resulting from the assumption of a continuum model, the ratio of atomic number density ρ_r is, therefore, specifically considered in this study. We notice that the modified continuum-atomistic model is similar to the previous literatures proposed by Cheng and Xu,[11] Amoruso *et al.*,[13] and Wang,[18] but we make some special modifications including the calculation of scaling coefficient ξ and the consideration of density effect. In Fig. 3, we show that the modified method indeed prevents the temperature jump problems and is relatively close to real-world physical situations by including the atomic density effect.

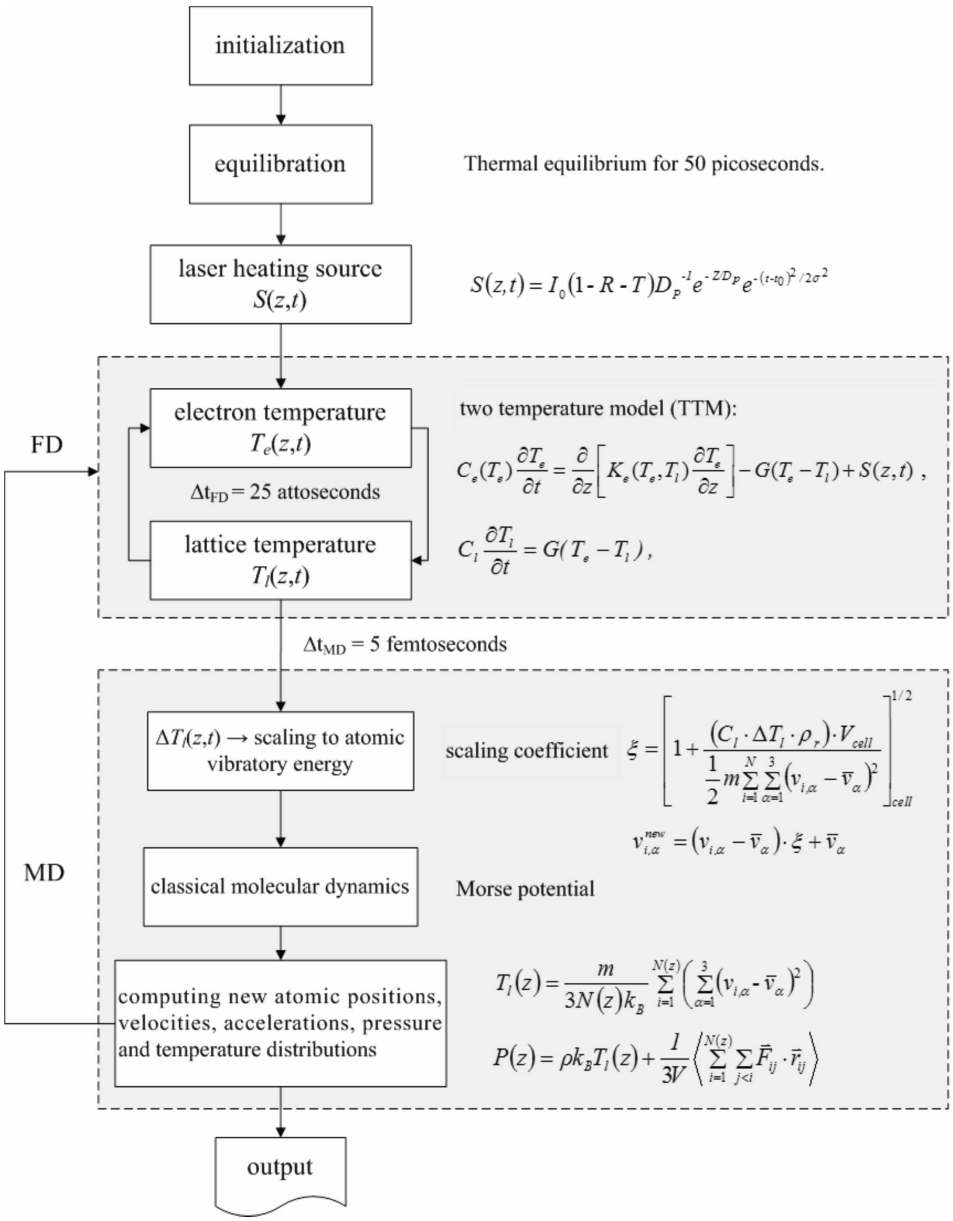

FIG. 2. Simulation flowchart for the modified continuum-atomistic approach.

III. RESULTS

A. Characterizations of annealing dynamics

The evolutionary behavior of electron temperature for an absorbed laser fluence of F_{abs}=45.0 mJ/cm^2 in the first 20 ps is computed to illustrate the initial thermal status, and the result is presented in Fig. 4. The transient profiles of electron temperature show that laser energy absorption does result in a steep increase of electron temperature near the irradiated surface. The electron temperature reaches a maximum of $T_e \sim 21\,700$ K at the end of the laser pulse, i.e., approximately at t=1.1 ps. Since high electronic heat conductivity leads to fast delivery of the incident laser energy within the target and results in rapid redistribution of electron heat from the radiated surface to the target in depth, the steep distribution of electronic temperature is quickly adjusted and becomes somewhat more uniform in distribution in the target after t=7 ps. The energy delivery in electronic subsystem progresses simultaneously in a relatively slow pace to transfer energy into the lattice subsystem due to the effect of electron-phonon coupling. After t=15 ps, the temperature equilibration between the electronic subsystem and the lattice subsystem is then achieved. The temporal and spatial evolutions of the lattice temperature in the irradiated target are carefully estimated and presented in Fig. 5, shown in the form of contour plots. The line in black depicts the transient position of a nanopore as a function of time. The lattice temperature is evaluated by the atomic vibratory velocity of the lattice subsystem as given in Eq. (7). The incident laser energy is transferred from hot electrons to the lattice, leading to an increase in initial lattice temperature. The difference in specific heat capacity between electrons and the lattice reflects that the lattice temperature increase is homogeneous and slow in pace as compared to that of electron temperature.

The lattice temperature reaches a maximum of approximately 2050 K at the vicinity of the radiated surface at t =15 ps, which is nearly equivalent to the time for thermal

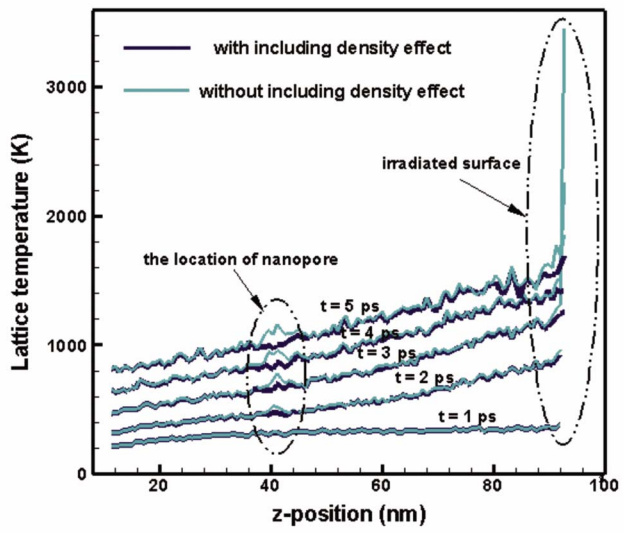

FIG. 3. (Color online) Effect of atomic density on lattice temperature for the first several picoseconds after laser heating. The marked regions also show the phenomena of "temperature jump."

equilibration between electrons and the lattice. The increase of lattice temperature at the vicinity of the radiated surface is estimated to be at a heating rate of order 10^{14} °C/s. High heating rate, at initial few picoseconds after the pulse laser heating, induces a particular heating mode of nearly constant volume, causing the buildup of high thermoelastic pressure. The condition is generally referred to as *stress confinement*.[36] The pressure contours are recorded and presented as a function of time and position in Fig. 6. Pressure is computed by using Eq. (8). The notion of pressure is positive for expansion and is negative for compression. The pressure wave is propagated into the target with maximum amplitudes in the order of −7.0 GPa. It is interesting to note that maximum pressure is built around the location of a nanopore at approximately $\sim 3.5D_p$ beneath the irradiated surface. The propagation velocity of the shock wave is estimated to be 4517 m/s from the simulation. The velocity is close to the experimental longitudinal-wave sound velocity of 4760 m/s for the annealed copper material.[37] When the pressure wave passes the pore, the wave intensity is weakened obviously because of the increase of impediment for the pore.

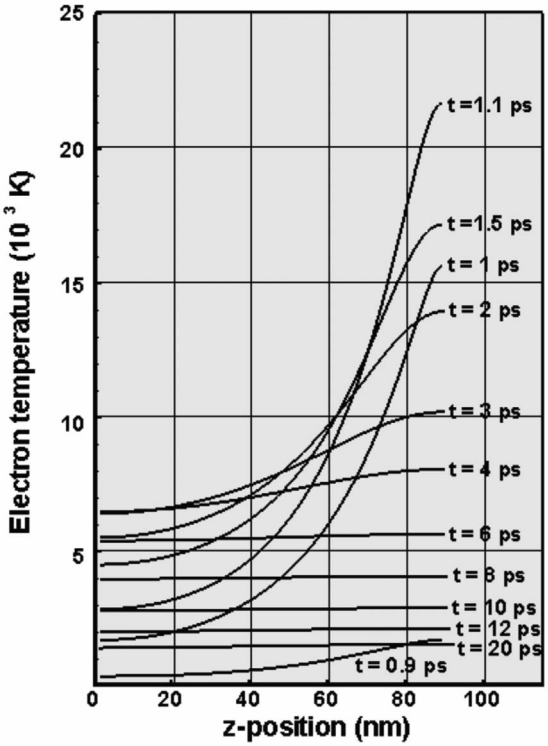

FIG. 4. The profiles of electron temperature as function of time and z position, by an absorbed laser fluence of F_{abs}=45.0 mJ/cm^2.

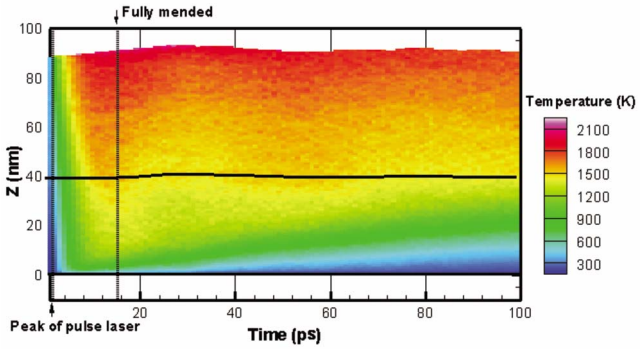

FIG. 5. (Color online) Contour plots of lattice temperature for MD simulation of laser annealing irradiated with a 100 fs laser pulse at an absorbed fluence of 45.0 mJ/cm^2. The black line depicts the transient position of the nanopore (ϕ=3 nm and Z_D=50.4 nm).

After the collapse at a nanopore, the compressive stress is gradually released and local tensile stress slowly builds up in the vicinity of the pore. Once the intensity of local pressures finally reach its maximum of 4.0 GPa at approximately t =30 ps, a pressure variation takes place from tensile yellow to compressive green, as depicted in Fig. 6, so that extra irradiated energy is quickly released via an equivalent stress balancing process between tension and compression. The alternation between compression and tension oscillates and quickly decays. This quick energy releasing process can result in an obvious anisotropic lattice distortion and a deformation near the mending pore.

Figure 7 shows the evolutions of atomic number density expressed as a function of time and position. The contour plot of atom density shows a feature of stripelike distribution for a typical FCC(100) crystal. The evolutions of atom density reflect the interplay of several crucial thermodynamic processes including the heat absorption inducing material expansion; the propagation and relaxation of pressure wave resulting in the alternate compression and expansion of a material; and the lattice slip motions leading to the changes of structural density. It is found that the trajectories of density show a negative curvature as the material is in the mode of compression, whereas the expansion corresponds to a positive curvature. The propagation of shock wave leads to a drastic increase of local density at the initial heating stage. In the following, the pressure wave arrives at the location of the nanopore and this results in the increase of compression stress in the vicinity of the pore. The compression stress

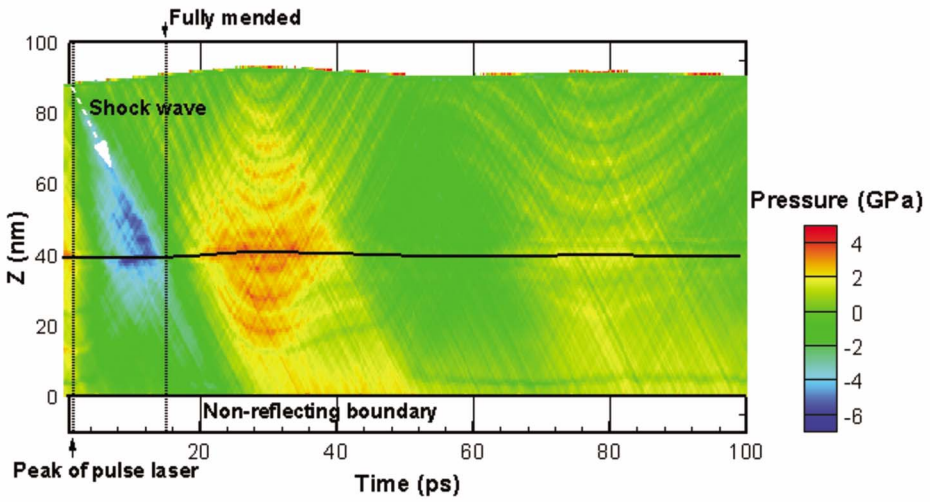

FIG. 6. (Color online) Contour plots of lattice pressure for MD simulation of laser annealing irradiated with a 100 fs laser pulse at an absorbed fluence of 45.0 mJ/cm^2. The black line depicts the transient position of the nanopore (ϕ=3 nm and Z_D=50.4 nm).

further induces a large number of lattice slip motions around the pore, and therefore, significantly contributes to the mending of the nanopore by pressure-induced structural mending. The nanopore structural changes reflected in Fig. 7 show that the atomic density is rapidly increased to a high level during the period when the shock wave impinges on the pore structure, and that the stripelike trajectories become dramatically vague due to a large number of lattice slips. Afterward, the density of the mended region is gradually decreased following the relaxation of the pressure wave. The density profile is then shown in an oscillatory mode due to the material thermal expansion, cooling, and the stress field evolutions. As can be seen from Figs. 5–7, the motion of radiated surfaces of the target consists of the initial thermal expansion of the material, followed by the dissipated oscillations due to the pressure relaxations and gradual cooling of the target. These involved phenomena further demonstrate that the structural changes are closely related to the evolution of the annealing dynamics.

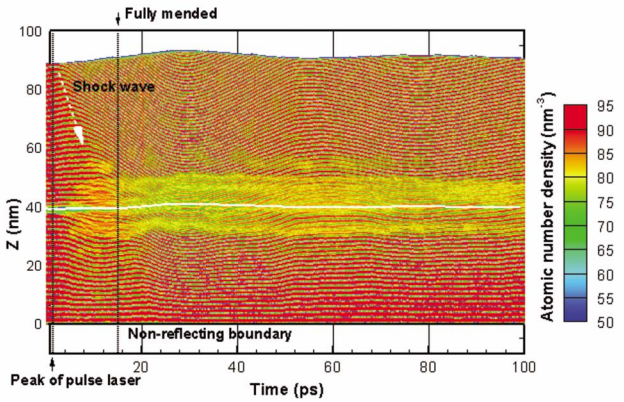

FIG. 7. (Color online) Contour plots of atomic number density for MD simulation of laser annealing irradiated with a 100 fs laser pulse at an absorbed fluence of 45.0 mJ/cm^2. The white line depicts the transient position of the nanopore (ϕ=3 nm, and Z_D=50.4 nm).

B. Pressure-induced heterogeneous nucleation of dislocation

Figure 8 shows the pressure-induced heterogeneous nucleation of dislocation in the vicinity of the pore surface during the initial period of t=5–8 ps. In order to clearly quantify the dislocation structure, a quantity, *slip vector*, S^α, is defined and given as[38]

$$S^\alpha = -\frac{1}{n_s}\sum_{\beta\neq\alpha}^{n}(x^{\alpha\beta} - X^{\alpha\beta}), \tag{11}$$

where n is the number of atoms in the nearest neighborhood of atom α, n_s is the number of atoms that is slipped away among n, and $x^{\alpha\beta}$ and $X^{\alpha\beta}$ represent the vector differences of atoms a and b at current and reference positions, respectively. The reference position vector is the original atomic position vector before deformation (i.e., without any mechanical stress).[38] If the estimated modulus of slip vector in copper is $|\mathbf{S}^\alpha|$=1.48 Å, then it can be realized by a $\{111\}\langle 112\rangle$ partial dislocation. Similarly, 2.56 Å can be realized as a perfect $\{111\}\langle 110\rangle$ glide. Here, the magnitude of a slip vector is used as an index to signal the degree of severe deformation. The components of slip vector can also be used to identify whether specific partial dislocation is nucleated on a $\{111\}$ plane in each possible direction. In Fig. 8, the atoms in faulty stacking regions are colored based on the magnitude of the slip vector, $|\mathbf{S}^\alpha|$. Partial dislocation is represented in mazarine, full dislocation in green, and atom slip over a unit dislocation in yellow and red. The faulty stacking regions are bounded by partial dislocations, which are heterogeneously nucleated from the pore surface and propagated along with different $\{111\}$ planes at t=5–8 ps. The increase of pressure can further induce shear slip along $\{111\}\langle 112\rangle$ and partial dislocation on $\{111\}$ glide planes, and then the dislocation propagates to encircle the whole pore surface to form a rhombus dislocation structure approximately at t=8 ps. These nucleated defects lie on close-packed $\{111\}$ crystallographic planes, which are the energetically preferred slip planes in the FCC lattice.

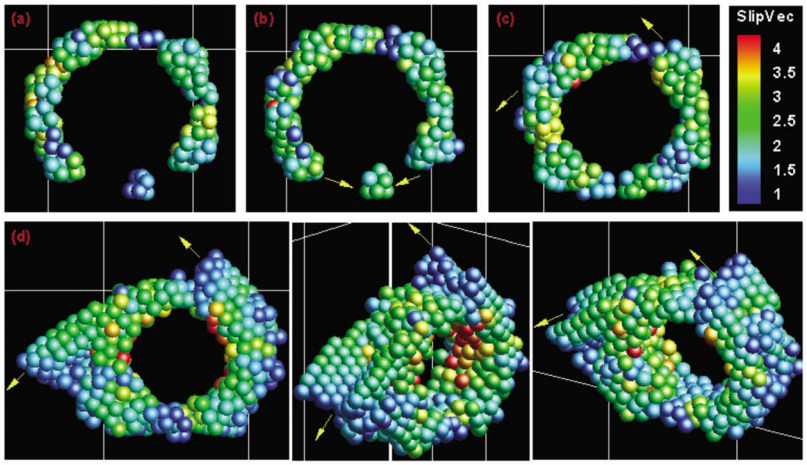

FIG. 8. (Color online) The incipient heterogeneous nucleation of dislocation around the pore surface at different times of (a) $t=5$, (b) $t=6$ ps, (c) $t=7$, and (d) $t=8$ ps, while in (d) the dislocation structures are shown along different viewpoints. Atoms are color coded by the value of $|\mathbf{S}^{\alpha}|$ in angstrom. Arrows denote the growth directions of dislocation structures.

Figure 9 shows the temperature, normal stress, mean-square displacement of atoms (MSD), and relative diameter change of the pore expressed as a function of time. It is noted that the evaluated normal stress is not the stress right at the pore surface since the pore surface is shrunk and fully mended fast. In Fig. 9, the normal stress is an averaged quantity of space and time, and it is evaluated in terms of a specific flexible control volume centered at and around the pore region. The *Roman number* indicates three different phases in the lattice mending process. These include (I) incubation of dislocation nucleation, (II) pressure-induced dislocation propagation and plastic deformation, and (III) lattice recovery and reconstruction via thermal diffusion. Phase (I) is a stress incubation stage where the heterogeneous nucleation of dislocation is induced by a critical shear stress in the vicinity of the pore surface. The distinct nucleation of $\{111\}\langle 112\rangle$ partial dislocation is closely monitored near the pore surface after $t=5.0$ ps. Phase (I) is generally referred to as the incubation of dislocation nucleation. The trajectory of computed normal stress indicates that the initial value of 2.8 GPa is equivalent to a cylindrical surface-induced tension stress in such a discrete molecular system. The normal stress is steeply increased with the propagations of shock wave at $t=8-14$ ps, leading to a large number of dislocations, so that the nucleation and multiplication take place as shown in Figs. 8 and 10. The maximum normal stress around the pore is −9.5 GPa, which is established at $t=12$ ps. Meanwhile, the pore diameter is evaluated to decrease by 48%, and the corresponding volumetric mended rate by approximately 73%. The result indicates that the pore can possibly be mended in the buildup stage of maximum compression stress.

The melting temperature of copper materials based on the Morse potential calculation is evaluated at 1850–1890 K for surface melting and at 1980–2040 K for bulk melting. The temperature trajectory of the pore, as given in Fig. 9, is rapidly increased from the room temperature of 300 K to its maximum around 1500–1600 K. The temperature trajectory around the pore indicates that the operation of pore mending was undergone a solid-state structural transition process.

Since MSD provides information on atomic self-diffusion and the relation of macroscopic transport coefficients with molecular motion, it can, thus, be adequately employed here to characterize the state of atomic motion around the pore region in terms of the slope variations. The MSD in Fig. 9 is the computational result that is evaluated in terms of a flexible specific control volume centered at and around the pore. The MSD is thus defined as

$$\mathrm{MSD} = \frac{1}{N}\left\langle \sum_{i}^{N} [\vec{r}_i(t) - \vec{r}_i(0)]^2 \right\rangle, \tag{12}$$

where $\vec{r}_i(t)-\vec{r}_i(0)$ denotes the distance that the vector traveled for molecule i over a certain time interval of length t, and the squared magnitude of this vector is averaged (as indicated by the angle brackets) over many such time intervals. The MSD curve clearly depicts the pronounced behavior of phase (II), which is quadratic in the early stage and linear in the middle to final stage. The behavior for the slope variation of the MSD is similar to that of the Lennard-Jones fluids in the gaseous state.[34] However, it should be realized that the behavior is not induced by the fluid motions. The behavior indeed results from the evolution of local dislocation induced by the shock-wave front-end pressure. The

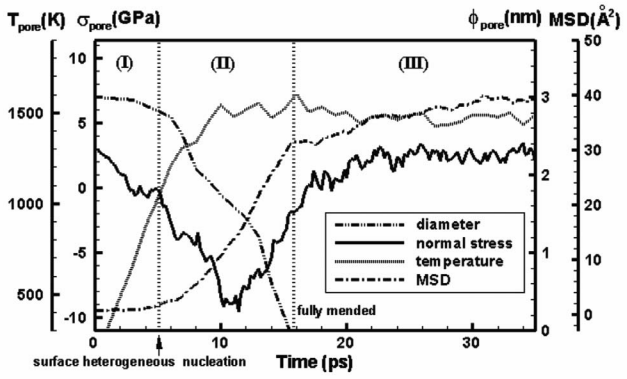

FIG. 9. Temporal evolution of temperature, normal stress (σ), MSD, and relative diameter change of the nanopore ($\phi=3$ nm and $Z_D=50.4$ nm) as function of time, performed by a 100 fs laser pulse at an absorbed fluence of 45.0 mJ/cm^2. The Roman number denotes the three different mending stages (see text).

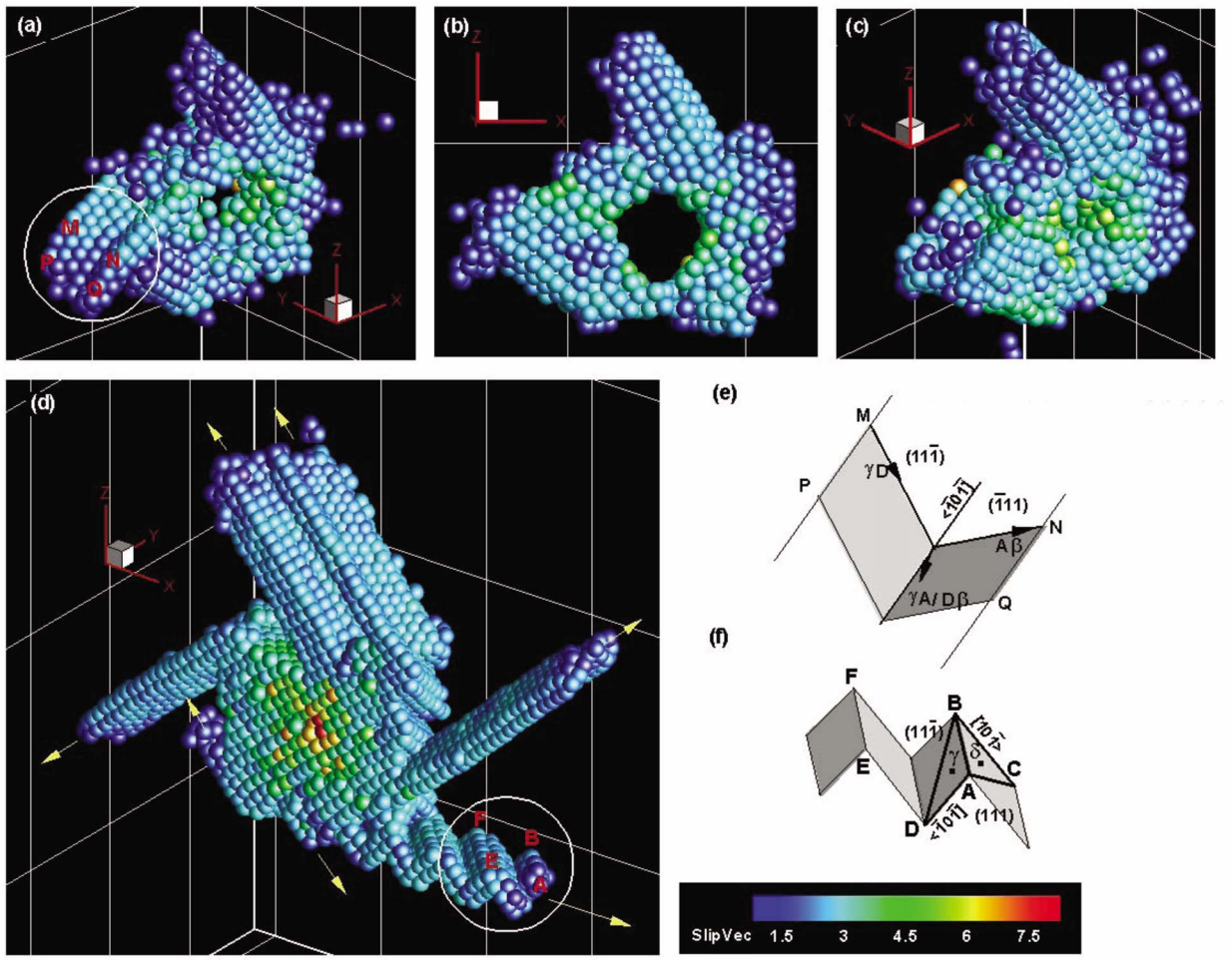

FIG. 10. (Color online) Dislocation structures at different times of phase (II) along different viewpoints: (a) view along $[11\bar{1}]$ at $t=9$ ps, (b) view along [010] at $t=10$ ps, (c) view along $[11\bar{1}]$ at $t=12$ ps, and (d) view along $[\bar{1}1\bar{1}]$ at $t=30$ ps for phase III. (e) and (f) denote the activated slip system (bold line) associated with the Thompson tetrahedron for the encircled dislocation zones of Figs. 9(a) and 9(d), respectively. Atoms are color coded by $|\mathbf{S}^{\alpha}|$ in angstrom. Arrows denote the growth directions of dislocation structures.

rapid dislocation motion from the beginning of the heterogeneous nucleation up to the end of complete pore mending (i.e., $t\sim 15.5$ ps) leads to a steep increase in MSD. After that, the MSD curve is changed abruptly into a slightly fluctuating line of flatte slope, indicating that the pore is phenomenologically fully mended and the remaining MSD is just for lattice reconstruction. The turning point of the MSD curve can thus be used to identify the time when the pore is phenomenologically fully mended. Phase (II), from the initial dislocation nucleation up to the full mending of the pore, can thus be realized as a stage of pressure-induced dislocation propagation and plastic deformation.

C. Dislocation emissions and recovery phase

Figures 10(a)–10(c) shows the dislocation structures in different viewpoints at different times of phase (II). It is obvious that the dislocation patterns for two different branches of the stair rod are rapidly developed at $t=9$ ps. Each branch of the stair rod consists of two different dislocation orientations on different {111} planes. An unstable dislocation structure is given and marked in the circularized zone of Fig. 10(a). The circularized dislocation structure is reproduced by means of a Thompson tetrahedron as depicted in Fig. 10(e). Both the internal stress and the energy favored deduction can lead to partial dislocations (γD and $A\beta$) detached from primary glide systems after initial glide. The two partial dislocations will interact with each other along the conjunctive line of their respective {111} planes to converge on that $[\bar{1}0\bar{1}]$ line at a certain distance from the pore. The aforementioned reaction creates the Burgers vector lying on the (010) plane that is not in a close-packed slip plane. Therefore, this junction acts as a barrier to impede further glide on both the mobile {111} planes, forming a sessile stair-rod junction with the configuration of an obtuse angle at 109.5°. The reaction can be further expressed as

$$\gamma D + A\beta \rightarrow \gamma A/D\beta, \tag{13}$$

or as expressed in energy form

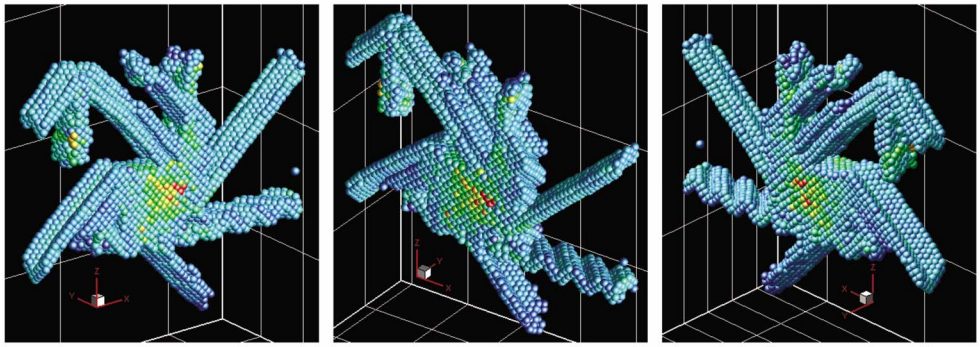

FIG. 11. (Color online) Snapshots of dislocation emission for an annealed structure along different viewpoints at $t=110$ ps; left, middle, and right images denote views along $[11\bar{1}]$, $[\bar{1}1\bar{1}]$, and $[1\bar{1}\bar{1}]$, respectively. Atoms are color coded by slip vector modulus $|\mathbf{S}^{\alpha}|$ as in Fig. 9; only dislocation atoms are shown.

$$6a_0^2/36 + 6a_0^2/36 < 20a_0^2/36, \tag{14}$$

where $\gamma A/D\beta$ represents a vector of twice the length of the vector connecting the midpoint of γA to the midpoint of $D\beta$. However, based on the squared criterion of the Burgers vector,[39,40] the dislocation energy of the reaction from Eqs. (13) and (14) is not reduced, indicating that the reactant is unstable. Therefore, it can be observed that the unstable dislocation rapidly recedes and is annihilated, as shown in Figs. 10(b) and 10(c).

In phase (III), the local tensile stress is generated around the pore region due to the relaxation of compressed pressure energy stored in target materials. The sustained pressure relaxation leads to a rapid swelling of the target along the z direction by an expansive strain rate of 2.2×10^9 s^{-1}. The expansive dynamics provides considerable mechanical work and, consequently, transfers sufficiently applied stress and leads to further lattice glides on activated mobile planes. Figure 10(d) shows the corresponding dislocation structure of phase (III) at $t=30$ ps. The structural expansion dynamics and associated tension stress lead to a dramatic disrupted emission of the dislocation structure. The structural emission of the dislocation originated from the nucleation of partial dislocations that are adjacent to the earlier stacking faults. Emissions also propagate along the initial easy glide planes. In order to further understand the interactions of dislocations in Fig. 10(d), the corresponding activated slip system associated with the Thompson tetrahedron on each mobile plane of the circularized stair-rod dislocation is presented in Fig. 10(f). The stair-rod dislocation can be attributed to the reactions of Lomer–Cottrell,[40] in which two perfect dislocations are further dissociated into individual partial dislocations along the adjacent line of their respective {111} glide planes to eventually construct a more stable converged partial dislocation structure. The partial dislocations, γB and $B\delta$, are detached from the primary glide systems, yielding the reaction along the interaction line $[\bar{1}10]$ to form a new reactant that can be described as

$$\gamma B + B\delta \rightarrow \gamma\delta, \tag{15}$$

or as expressed in energy form

$$6a_0^2/36 + 6a_0^2/36 > 2a_0^2/36. \tag{16}$$

The new dislocation reactant, $\gamma\delta$ (i.e., $1/6[110]$), lies on the plane (001) and is perpendicular to the moving direction of dislocation, indicating that it has a pure screw character. It can be seen in terms of Burgers vectors that the junction is sessile and has a configuration of acute angle at 70.5° between its two glide planes. Since the plane (001) is not a close-packed slip plane, this junction functions as a strong barrier to impede further glide on each {111} slip plane, yielding a so-called local strain-hardening effect. By employing the squared criterion of the Burgers vector, one can also realize that the reaction of Eq. (16) is also energetically favorable.

Based on the analyses of thermodynamics states and dislocation evolution, one can verify that the multiplication, coalescence, and annihilation of dislocation are closely related to the annealing dynamics. The internal stress and alternation of compression and expansion stress are also closely related to the change of dislocation to be grown, blocked, or receded. The atomic slips and dislocation motions will gradually dissipate away most of the mechanical work by reducing the systems potential energy to enhance structural stabilization. The dislocation motion will also be gradually mitigated and, eventually, a stacking fault structure, as given in Fig. 11, is left. Note that, at the core zone of the mended pore, a large slip vector modulus ($|\mathbf{S}^{\alpha}|>10$ Å) is possible due to the atoms' slip over several units of dislocation. In the mended region, the deformed lattice is recovered and reconstructed by means of a long annealing process via the introduction of residual thermal energy. These stacking faults can then be reconstructed to well-organized least-defects crystalline structures. Thus, phase (III) can be realized as the lattice recovery stage through thermal diffusion.

Since the atomic potential energy (APE) is closely related to structural changes, one can use it to indicate the structural defect and recovery. In Fig. 12, the APE is estimated and plotted for deferent time evolutions. It is obvious that the dislocation nucleation and/or defect formation will occur when the potential energy is above the value between −2.6 and −3.0 eV for a copper material.[41,42] Therefore, in Fig. 12, the right panels show the specific atoms that have potential

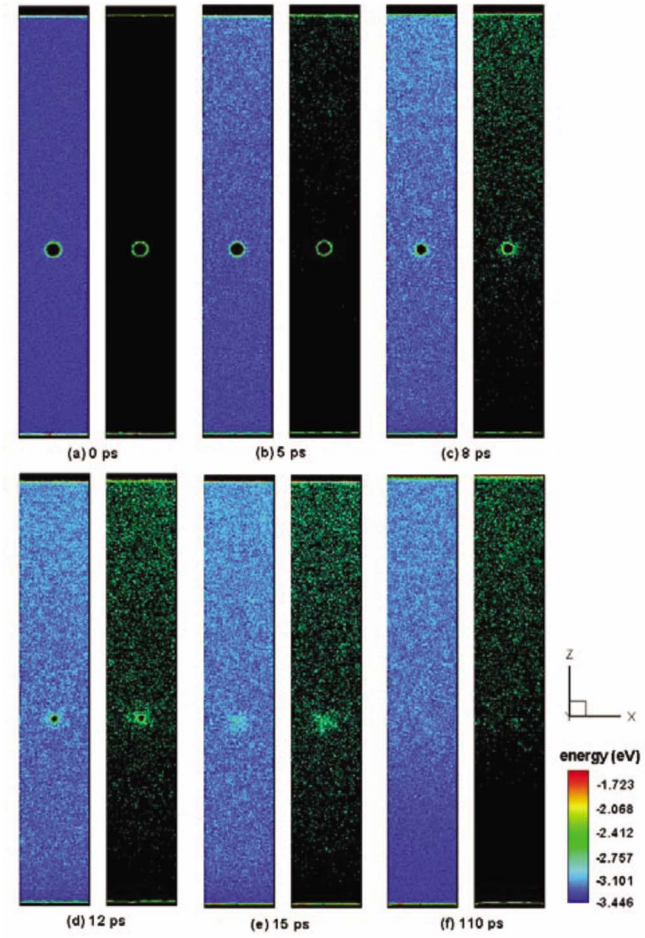

FIG. 12. (Color online) The evolutions of annealing configurations at different mending and recovery phases. Atoms are color coded by the values of the potential energy in eV; mazarine represents a nearly perfectly aligned crystal. The left images show all atoms for different times; the right images show only the atoms with high potential energy above −2.872 eV for different times.

energy greater than −2.872 eV, whereas the left panels are for all atoms evolved at different time histories. It indicates that the system energy is relatively stable at the initial stage of phase (I). Subsequently, the APE gradually becomes unstable as the shock wave propagates from the irradiated surface to the depth of the target. It is also found that the potential energy around the pore is generally increased in phase (II) due to the increase of local pressure and the growth of dislocation. Especially, the APE is rapidly increased from the pore surface at $t=8$ ps, indicating that the dislocations are rapidly nucleated and propagated. Finally, the APE is gradually recovered to a stable situation in phase (III), indicating the smooth structure recovered.

IV. SUMMARY AND CONCLUDING REMARKS

The microscopic nanopore mending process via femtosecond pulse laser annealing is studied in this paper by using the modified continuum-atomistic simulation. Several conclusions can be drawn from the present study as follows:

(1) Analyses show that the structural mending of the pore originates from the heterogeneous nucleation of a dislocation from the pore surface. The pressure-induced multiple lattice glides play a significant role on the fast mending process of a nanopore. Through laser-induced shock pressure and the solid-state mending devices, one can enhance the associated FLA defect mending functions for time saving and low energy consumption.

(2) The structure after annealing shows that the mended regions have well-organized periodic lattice alignments, indicating that good quality crystalline features can be achieved and that the postfinishing treatment can be minimized or even eliminated by using the present mending approach.

(3) The stair-rod-type sessile dislocation acts as a strong barrier to prevent further glide on slip planes and, thus, lead to a local strain-hardening effect. This effect becomes very helpful for the characterization of the laser-induced surface-hardening mechanism. The approach can therefore be enhanced to produce wear-resistant patterns on discrete surfaces of advanced functional materials.

(4) The onset for three typical lattice mending phases is identified via the evolutions of microscopic dislocation and the slope change of the MSD curve. The application of a MSD diagram proposed in this paper is an effective device to identify the time when the pore is phenomenologically fully mended.

(5) The modified continuum-atomistic method, by taking into consideration the density effect, is proposed to avoid an erroneous estimate of the energy deposition resulting from the assumption of a continuum model. The above proposed model can be further modified and applied to estimate the critical mending threshold and the mending depth for various nanodefects as well.

ACKNOWLEDGMENT

The authors gratefully acknowledge the support provided to this research by the National Science Council of the Republic of China under Grant No. NSC95-2221-E-006-397.

*Author to whom any correspondence should be addressed. FAX: +886-6-2352973; hylai@mail.ncku.edu.tw

[1] J. M. Shieh, Z. H. Chen, B. T. Dai, Y. C. Wang, A. Zaitsev, and C. L. Pan, Appl. Phys. Lett. **85**, 1232 (2004).

[2] J. A. Sharp, N. E. B. Cowern, R. P. Webb, K. J. Kirkby, D. Giubertoni, S. Gennaro, M. Bersani, M. A. Foad, F. Cristiano, and P. F. Fazzini, Appl. Phys. Lett. **89**, 192105 (2006).

[3] S. K. Sundaram and E. Mazur, Nat. Mater. **1**, 217 (2002).

[4] G. G. Bentini, C. Cohen, A. Desalvo, and A. V. Drigo, Phys. Rev. Lett. **46**, 156 (1981).

[5] Y. Hirayama and M. Obara, J. Appl. Phys. **97**, 064903 (2005).
[6] D. A. Reis, K. J. Gaffney, G. H. Gilmer, and B. Torralva, MRS Bull. **31**, 601 (2006).
[7] C. L. Cleveland, U. Landman, and R. N. Barnett, Phys. Rev. Lett. **49** 790 (1982).
[8] H. Hakkinen and U. Landman, Phys. Rev. Lett. **71**, 1023 (1993).
[9] C. Schafer, H. M. Urbassek, and L. V. Zhigilei, Phys. Rev. B **66**, 115404 (2002).
[10] D. S. Ivanov and L. V. Zhigilei, Phys. Rev. B **68**, 064114 (2003).
[11] C. Cheng and X. Xu, Phys. Rev. B **72**, 165415 (2005).
[12] H. Y. Lai, P. H. Huang, and T. H. Fang, Appl. Phys. A: Mater. Sci. Process. **86**, 49 (2007).
[13] S. Amoruso, R. Bruzzese, X. Wang, N. N. Nedialkov, and P. A. Atanasov, Nanotechnology **18**, 145612 (2007).
[14] M. I. Kaganov, I. M. Lifshitz, and L. V. Tanatarov, Sov. Phys. JETP **4**, 173 (1957).
[15] S. I. Anisimov, B. L. Kapeliovich, and T. L. Perel'man, Sov. Phys. JETP **39**, 375 (1974).
[16] K. Lu and Y. Li, Phys. Rev. Lett. **80**, 4474 (1998).
[17] B. Rethfeld, K. Sokolowski-Tinten, D. von der Linde, and S. I. Anisimov, Phys. Rev. B **65**, 092103 (2002).
[18] X. Wang, ASME Trans. J. Heat Transfer **126**, 355 (2004).
[19] W. D. Callister, *Materials Science and Engineering: An Introduction* (Wiley, New York, 1990).
[20] J. C. Ion, *Laser Processing of Engineering Materials: Principles, Procedure and Industrial Application* (Elsevier, New York/ Butterworth-Heinemann, Amsterdam, 2005).
[21] C. Schafer, H. M. Urbassek, L. V. Zhigilei, and B. J. Garrison, Comput. Mater. Sci. **24**, 421 (2002).
[22] M. P. Allen and D. J. Tildesley, *Computer Simulation of Liquids* (Oxford University, New York, 1987).
[23] D. J. Evans, W. G. Hoover, B. H. Failor, B. Moran, and A. J. C. Ladd, Phys. Rev. A **28**, 1016 (1983).
[24] T. Q. Qiu and C. L. Tien, J. Heat Transfer **115**, 835 (1993).
[25] T. Q. Qiu and C. L. Tien, Int. J. Heat Mass Transfer **37**, 2789 (1994).
[26] C. F. Gerald and P. O. Wheatley, *Applied Numerical Analysis* (Addison-Wesley, New York, 1997).
[27] D. R. Lide, *CRC Handbook of Chemistry and Physics* (Chemical Rubber, Washington, 2004).
[28] D. E. Gray, *American Institute of Physics Handbook* (McGraw-Hill, New York, 1972).
[29] M. Bonn, D. N. Denzler, S. Funk, M. Wolf, S. S. Wellershoff, and J. Hohlfeld, Phys. Rev. B **61**, 1101 (2000).
[30] S. I. Anisimov, B. Rethfeld, Y. S. Lee, and M. C. Downer, Proc. SPIE **192**, 3093 (1997).
[31] C. Kittel, *Introduction to Solid State Physics* (Wiley, New York, 1996).
[32] S. Amoruso, R. Bruzzese, X. Wang, N. N. Nedialkov, and P. A. Atanasov, J. Phys. D **40**, 331 (2007).
[33] W. K. Liu, J. M. Yuan, and S. H. Lin, Phys. Rev. A **60**, 1363 (1999).
[34] R. C. Lincoln, K. M. Koliwad, and P. B. Chate, Phys. Rev. **157**, 463 (1967).
[35] J. M. Haile, *Molecular Dynamics Simulation: Elementary Methods* (Wiley, New York, 1992).
[36] G. Paltauf and P. E. Dyer, Chem. Rev. (Washington, D.C.) **103**, 487 (2003).
[37] C. Weast Robert, *CRC Handbook of Chemistry and Physics* (CRC, Boca Raton, FL, 1988).
[38] J. A. Zimmerman, C. L. Kelchner, P. A. Klein, J. C. Hamilton, and S. M. Foiles, Phys. Rev. Lett. **87**, 165507 (2001).
[39] J. P. Hirth and J. Lothe, *Theory of Dislocations* (Wiley, New York, 1982).
[40] D. Hull and D. J. Bacon, *Introduction to Dislocations* (Oxford University, New York, 1984).
[41] C. Ji and H. S. Park, Nanotechnology **18**, 3057704 (2007).
[42] C. Ji and H. S. Park, Appl. Phys. Lett. **89**, 181916 (2006).